

**Transition to three dimensional flow in thermal convection with spanwise rotation**K. Lüdemann and A. Tilgner<sup>1</sup>*Institute of Astrophysics and Geophysics, University of Göttingen,  
Friedrich-Hund-Platz 1, 37077 Göttingen, Germany*

(Dated: 12 May 2022)

We investigate by direct numerical simulation Rayleigh-Bénard convection in a rotating rectangular cell with rotation vector and gravity perpendicular to each other. The flow is two dimensional near the onset of convection with convection rolls aligned parallel to the rotation axis of the boundaries. At a sufficiently large Rayleigh number, the flow becomes unstable to three dimensional disturbances which changes the scaling of heat transport and kinetic energy with Rayleigh number. The mechanism leading to the instability is identified as an elliptical instability. At the transition, the Reynolds and Rossby numbers  $Re$  and  $Ro$  based on the kinetic energy of the flow are related by  $Re \propto Ro^{-2}$  at small  $Ro$  with a geometry dependent prefactor.

PACS numbers: 47.27.-i, 47.32.Ef, 47.27.te

## I. INTRODUCTION

Two experiments were recently built which place a thermal convection cell in a centrifuge. The boundary near the axis of the centrifuge is cooled while the opposite boundary is heated. The rotation rate of the centrifuge is fast enough so that the centrifugal acceleration acts as an effective gravity inside the convection cell and the Earth's gravitational field becomes negligible. The experiment by Jiang *et al.*<sup>1</sup> uses liquids as working fluids and relies on a large rotation rate to generate large Rayleigh numbers. The intention of the experiment by Menaut *et al.*<sup>2</sup> on the other hand is to study compressible convection and uses gas as convecting fluid.

In addition to creating a large effective gravity, the rotation also introduces a Coriolis acceleration which promotes 2D flow structures in geostrophic balance. The centrifuged convection cells may be regarded as models of the equatorial regions of the Earth's core or some deep planetary atmosphere in which buoyancy drives columnar convection rolls aligned with the rotation axis of the planet. Strict geostrophic balance requires all terms in the momentum equation apart from the pressure and Coriolis terms to be negligible. Viscosity becomes important in Ekman layers adjacent to boundaries perpendicular to the rotation axis so that the flows in the experiments are never exactly 2D. However, these deviations from 2D tend to zero for the Ekman number tending to zero so that we will associate the experimental flows in nearly geostrophic equilibrium with 2D flows. An important issue in connection with both the planetary application and the laboratory experiments is to know under which circumstances the geostrophic equilibrium holds and under which circumstances it is replaced by 3D flow. The present paper investigates the stability limit of the geostrophic flow.

It is frequently assumed that geostrophic equilibrium is destroyed as soon as the Rossby number exceeds some critical value. Nonlinear terms must be responsible if a flow in geostrophic equilibrium becomes unstable to 3D flows, and the Rossby number quantifies the ratio of the advection term in the momentum equation to the Coriolis term. However, it was found that for rotating convection in a plane layer rotating about an axis perpendicular to the layer, the Rossby number based on the actual flow velocities does not provide us with a criterion to predict when the flow departs from the rotation dominated regime<sup>3,4</sup>. In rotating convection with spanwise rotation, Jiang *et al.*<sup>1</sup> also find that the transition

away from geostrophic equilibrium is not characterized by a critical Rossby number independent of other control parameters if the Rossby number is based on the free fall velocity. These observations motivate us to find an accurate criterion for the disruption of geostrophic equilibrium for convection with spanwise rotation.

We will show that the mechanism responsible for the instability of geostrophic flows in convection with spanwise rotation is an elliptical instability. This type of instability was already shown to determine the stability of large scale circulations in convection<sup>5</sup> and to limit the size of convection rolls<sup>6</sup>. In the present application, we have to deal with a rotating frame of reference and we have to determine more accurately the properties of the elliptical instability to account for the observed variations of the critical Rossby number at the onset of instability of the geostrophic flow.

The next section describes the mathematical formulation on which the numerical simulations in the third section are based. The fourth section links the numerical results to the elliptical instability.

## II. THE MATHEMATICAL MODEL

We consider in a Cartesian coordinate system  $x, y, z$  a rectangular cell of size  $d$  along  $z$  and size  $L$  along  $x$  and  $y$ . The cell rotates about the  $y$ -axis at rate  $\Omega$ . A temperature difference  $\Delta T$  is applied to the boundaries perpendicular to  $z$ . The cell is filled with a fluid of density  $\rho$ , kinematic viscosity  $\nu$ , thermal diffusivity  $\kappa$ , thermal expansion coefficient  $\alpha$  and the effective gravitational acceleration in the cell is  $g$ . Introducing units of length, time, velocity and temperature as  $d, d^2/\kappa, \kappa/d$  and  $\Delta T$  and assuming the validity of the Boussinesq approximation, the equation of evolution for the non dimensional velocity  $\mathbf{v}(\mathbf{r}, t)$ , pressure  $p(\mathbf{r}, t)$  and temperature deviation from the static profile  $\theta(\mathbf{r}, t)$  read

$$\frac{\partial}{\partial t}\mathbf{v} + (\mathbf{v} \cdot \nabla)\mathbf{v} + 2\frac{\text{Pr}}{\text{Ek}}\hat{\mathbf{y}} \times \mathbf{v} = -\nabla p + \text{PrRa}\theta\hat{\mathbf{z}} + \text{Pr}\nabla^2\mathbf{v} \quad (1)$$

$$\frac{\partial}{\partial t}\theta + \mathbf{v} \cdot \nabla\theta - v_z = \nabla^2\theta \quad (2)$$

$$\nabla \cdot \mathbf{v} = 0 \quad (3)$$

with the control parameters

$$\text{Pr} = \frac{\nu}{\kappa}, \quad \text{Ra} = \frac{g\alpha\Delta T d^3}{\kappa\nu}, \quad \text{Ek} = \frac{\nu}{d^2\Omega} \quad (4)$$

and where hats denote unit vectors. In an experimental cell in a centrifuge, the effective acceleration  $g$  is due to the centrifugal acceleration and varies in space. This variation can be reduced by using a cell with a small ratio of cell size  $d$  over distance to the centrifuge axis. We treat  $g$  as a constant in our calculations to avoid a profusion of control parameters. The computational volume is inspired by the geometry of the experiment by Menaut *et al.*<sup>2</sup> and we use  $d/L = 2$  in all simulations. For consistency, we always select a Prandtl number of 0.7 representative of a gas.

The walls are assumed to be stress free so that flows near the onset of convection do not contain Ekman layers and are exactly 2D. The boundaries perpendicular to  $z$  have fixed temperature, whereas the other boundaries are treated as heat insulating walls.

The equations of evolution were approximated for their numerical simulation by a method optimized for graphical processing units solving the equations for a weakly compressible fluid<sup>7,8</sup> with speed of sound  $c$ . The speed of sound was adjusted so that the Mach number  $|\boldsymbol{v}|/c$  never exceeded 0.1 at any time and any point inside the flow, and the ratio of the time it takes sound waves to travel across the cell and the rotation period was small. The latter criterion requires<sup>8</sup>  $c^2 \gg (\text{Pr}/(2\pi\text{Ek}))^2$ . For the simulations presented here,  $c^2\text{Ek}^2 > 0.5$  in all cases. The numerical code implemented a finite difference method with fourth order centered finite differences for all terms except the non linear advection terms which were discretized by a third order upwinding scheme. The simulations were run on a uniform collocated grid with resolutions of up to  $256 \times 256 \times 512$  grid points in 3D and up to  $1024 \times 2048$  grid points in 2D. A third order Runge-Kutta scheme was used for time stepping. Some of the 2D simulations were also run with the spectral element method implemented in NEK5000.

### III. THE STABILITY LIMIT OF CONVECTION FLOWS

Global quantities like the total kinetic energy or the heat transport depend differently on control parameters in 2D and 3D flows. This is the reason why the transition from 2D to 3D is important in geophysical applications. It is also for this reason that the transition is easily detectable in experiments which cannot access the full velocity field as conveniently as numerical simulations.

We will consider three global averages extracted from the simulations. The first of these is the heat transport which is also the most important diagnostic in experiments. The

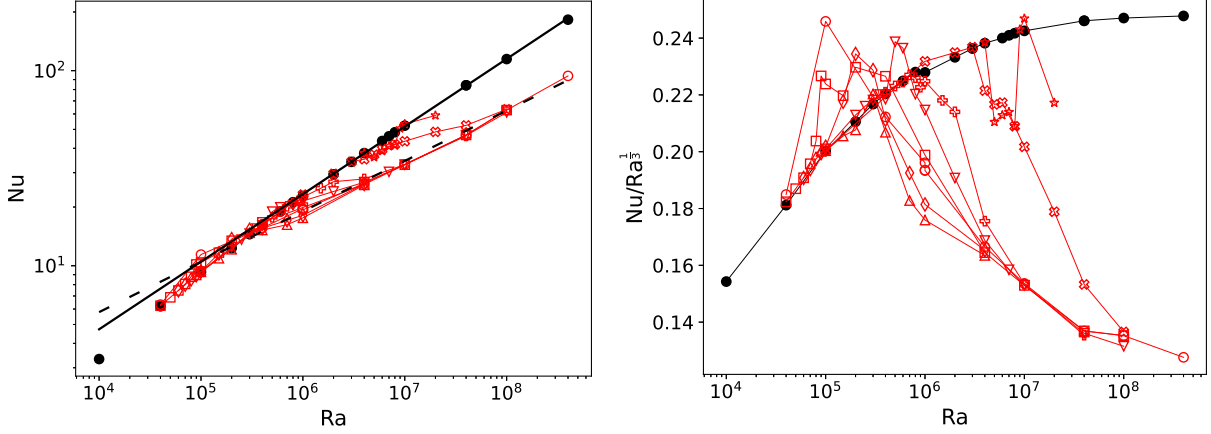


FIG. 1. Nu as a function of Ra for 2D (black dots) and 3D (empty red symbols) simulations for non rotating convection (circles),  $Ek = 10^{-2}$  (squares),  $7 \times 10^{-3}$  (diamonds),  $3 \times 10^{-3}$  (triangles up),  $10^{-3}$  (triangles down),  $4 \times 10^{-4}$  (plus),  $10^{-4}$  (x) and  $4 \times 10^{-5}$  (stars). The solid and dashed lines in the left panel indicate the power laws  $Nu = 0.18Ra^{0.35}$  and  $Nu = 0.54Ra^{0.26}$ , respectively, whereas the right panel shows the compensated Nusselt number  $Nu/Ra^{1/3}$ .

average heat flux, made dimensionless by dividing it by the heat conducted in the stationary motionless state, is represented by the Nusselt number Nu as the average over the boundary  $z = 0$  of area  $A$  of the normal derivative of the temperature field. If angular brackets  $\langle \dots \rangle$  denote the time average, Nu is given by

$$Nu = \left\langle \frac{1}{A} \int dx \int dy \partial_z T|_{z=0} \right\rangle. \quad (5)$$

The second quantity of interest is the Reynolds number Re based on the total kinetic energy defined as

$$Re = \frac{1}{Pr} \left\langle \frac{1}{V} \int dx \int dy \int dz |\mathbf{v}|^2 dV \right\rangle^{1/2} \quad (6)$$

where  $V$  is the total volume of the cell. The factor of Pr is necessary because velocity was made non dimensional with the thermal diffusivity. Finally, the most direct indicator of a transition from 2D to 3D flow is the anisotropy defined as the ratio of the energy in the velocity component parallel to the rotation axis and the energy in the components perpendicular to the axis of rotation:

$$\frac{\left\langle \frac{1}{V} \int dx \int dy \int dz v_y^2 dV \right\rangle}{\left\langle \frac{1}{V} \int dx \int dy \int dz (v_x^2 + v_z^2) dV \right\rangle}. \quad (7)$$

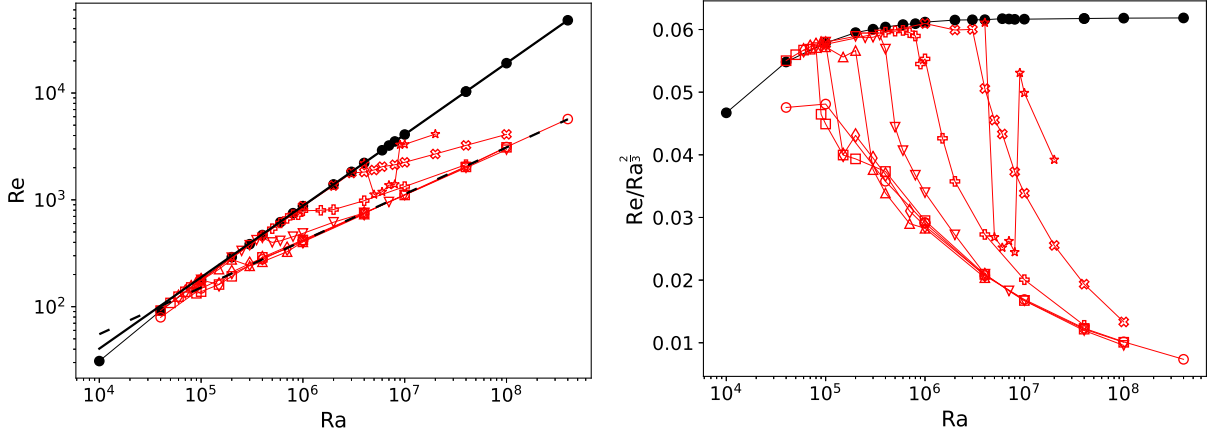


FIG. 2. Reynolds number  $Re$  (left panel) and compensated Reynolds number  $Re/Ra^{2/3}$  (right panel) as a function of  $Ra$  with the same symbols as in fig. 1. The solid and dashed lines in the left panel indicate the power laws  $Re = 0.09Ra^{0.67}$  and  $Re = 0.99Ra^{0.44}$ , respectively.

Figs. 1 and 2 show  $Nu$  and  $Re$  for two types of simulations. The first set of computations simulates 2D flows with streamlines confined to planes perpendicular to the rotation axis. The Coriolis term for these flows is conservative and can be absorbed into the pressure gradient so that these results are independent of  $Ek$ . Apart from lateral boundary conditions, these simulations are identical to older calculations. Wen *et al.*<sup>9</sup> investigate steady convection in 2D and find  $Nu$  and  $Re$  to scale as  $Nu \propto Ra^{1/3}$  and  $Re \propto Ra^{2/3}$  at constant lateral size of the convection rolls. For time dependent convection, van der Poel *et al.*<sup>10</sup> find  $Nu \propto Ra^{2/7}$  and Wang *et al.*<sup>11</sup> report similar exponents. The 2D runs in figs. 1 and 2 ended after some initial transient in a time independent state consisting of a single convection roll. Not surprisingly, the best fits to these results,

$$Nu = 0.18Ra^{0.35} \quad , \quad Re = 0.09Ra^{0.67}, \quad (8)$$

yield exponents compatible with Wen *et al.*<sup>9</sup>. As seen in the compensated plots, the exponents of Wen *et al.*<sup>9</sup> are approached at large  $Ra$ .

The second set of simulations in figs. 1 and 2 is fully 3D and hence dependent on  $Ek$ . One expects the dominant Coriolis term at low  $Ek$  and  $Ra$  to force the flow into a 2D geometry identical to the geometry enforced by construction in the first set of simulations. In that case, both sets of simulations must yield the same  $Nu$  and  $Re$ . As  $Ra$  is increased at constant  $Ek$ , the Coriolis term becomes negligible compared with the advection term

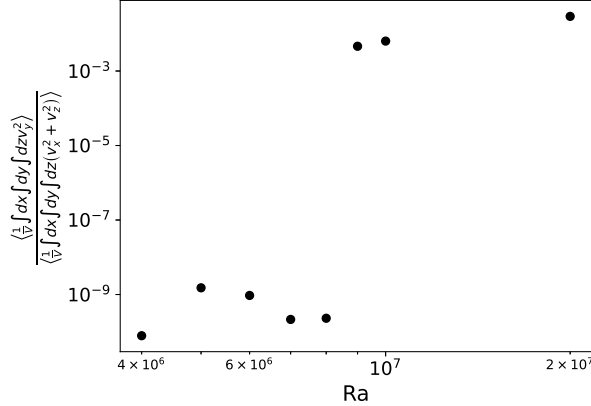


FIG. 3. The anisotropy (7) as a function of Ra for  $Ek = 4 \times 10^{-5}$ .

and all global quantities approach the values they have in the non rotating case. Pandey *et al.*<sup>12</sup> for instance report for 3D non rotating convection with free slip boundaries that  $Nu \propto Ra^{0.27}$ . It is straightforward to compare our simulations with existing results on non rotating convection. The situation is different for simulations which implement periodic lateral boundary conditions and allow a mean flow to appear which can significantly modify the convection<sup>13</sup>.

The expected qualitative behaviour is indeed observed in figs. 1 and 2 which show series of simulations in which Ra varies at several fixed Ek. At each of the Ek, the results are close to the 2D simulations at low Ra, whereas at large Ra, they asymptote to the scalings

$$Nu = 0.54Ra^{0.26} \quad , \quad Re = 0.99Ra^{0.44} \quad (9)$$

indicative of 3D convection. A smaller Ek requires a larger Ra to start the transition from 2D to 3D. The compensated plot for Nu shows a conspicuous overshoot of Nu at the transition for the larger Ekman numbers. The origin of this behavior was not investigated in detail because it disappears at small Ek.

It is inconvenient to locate the transition from 2D to 3D flows from the above results because the transition shows as a gradual deviation from a baseline (the 2D results) which is itself contaminated by numerical error. It is much more reliable to deduce the transition from the anisotropy (7) because this quantity is exactly zero for the 2D flows owing to the free slip boundaries. Fig. 3 shows as an example the anisotropy as a function of Ra for  $Ek = 4 \times 10^{-5}$ . The numerically evaluated anisotropy at small Ra for the supposedly 2D flows is not exactly zero but it is of the magnitude of round off errors and it is as small as

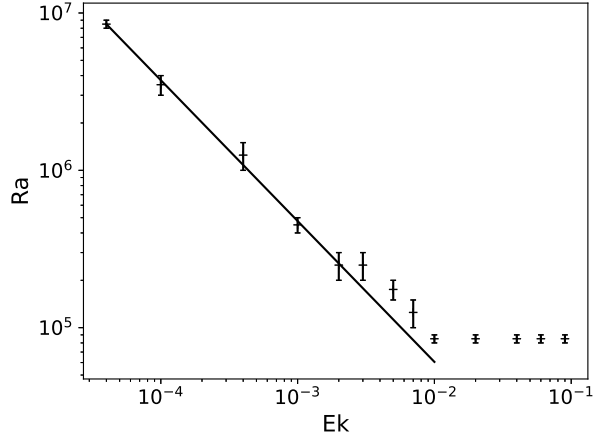


FIG. 4. The vertical bars indicate intervals of Ra in which the transition from 2D to 3D flows occurs as a function of Ek. The solid line is given by  $982\text{Ek}^{-0.9}$ .

it can be expected to be in a single precision floating point representation of real numbers. Plots like fig. 3 allow us to bracket the interval of Ra in which the transition occurs, the lower limit of the interval being the largest simulated Ra at which the anisotropy is of the size of round off errors and the upper limit being the smallest Ra at which the anisotropy is clearly different from zero. These intervals are shown as a function of Ek in fig. 4. At large Ek, rotation is irrelevant and the transitional Ra is independent of Ek, whereas for small Ek, the transition occurs approximately at a Rayleigh number given by  $982\text{Ek}^{-0.9}$ .

This observation leads to the hypothesis that buoyancy forces are irrelevant for the transition at low Ek. One can compare the characteristic time scales of the dynamics induced by rotation and buoyancy. The time scale for rotation, which manifests itself for example in the dispersion relation of inertial waves, is of course the inverse of the rotation rate  $1/\Omega$ . A characteristic time scale for buoyancy is the transit time of a parcel of fluid traversing the cell at free fall velocity,  $[d/(g\alpha\Delta T)]^{1/2}$ . The ratio of both,  $[g\alpha\Delta T/d]^{1/2}/\Omega = (\text{RaEk}^2/\text{Pr})^{1/2}$ , which may also be identified as a Rossby number<sup>14,15</sup>, is equal to 0.82 at  $\text{Ek} = 10^{-3}$  and equal to 0.066 at  $\text{Ek} = 10^{-5}$  at the transition. If this ratio is small, the motion of a fluid parcel changes under the influence of rotational effects on a time scale on which buoyancy is unable to modify its motion. Buoyancy therefore becomes irrelevant to the dynamics.

This motivates us to describe the transition with parameters independent of buoyancy. In isothermal flows, the transition from flows patterned by the Coriolis force to flows independent of rotation is usually thought to be governed by the Rossby number Ro defined



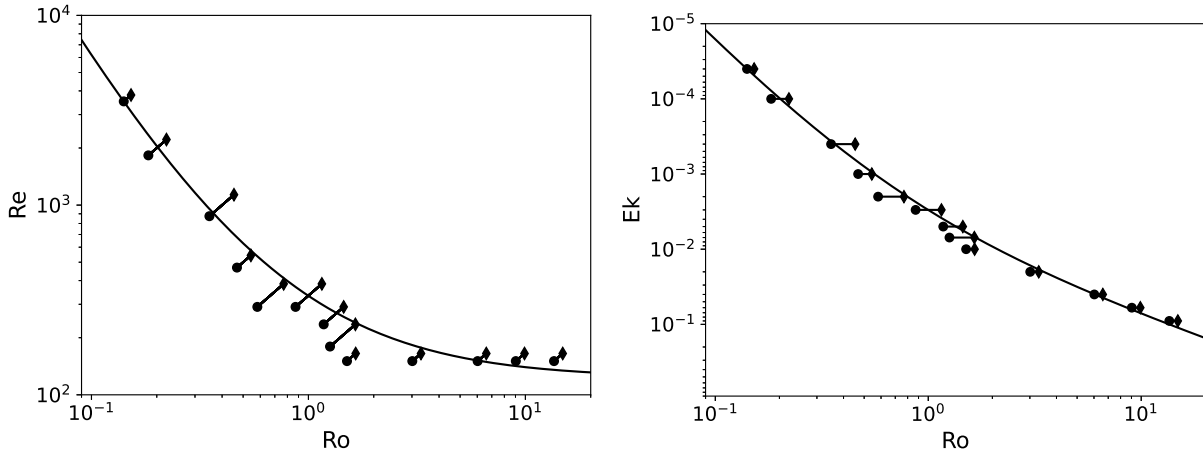


FIG. 5. Line segments crossing the stability limit of 2D flows in the  $(\text{Re}, \text{Ro})$ -plane (left panel). The continuous curve results from the stability analysis for an elliptical vortex with  $\beta = 0.78$  and  $k_{\parallel} = 2\pi$ ,  $k_{\perp} = \pi$ . The right panel shows the same data and the same curve in the  $(\text{Ek}, \text{Ro})$ -plane.

by  $\text{Ro} = \text{EkRe}$ . The intervals of  $\text{Ra}$  in fig. 4 containing the transition are translated into intervals of  $\text{Re}$  by simply reading off the  $\text{Re}$  for the  $\text{Ra}$  at the lower end of the interval from the 2D simulations, and by computing a Reynolds number by extrapolating the  $\text{Re}(\text{Ra})$  dependence of 2D flows to the Rayleigh number at the upper end of the intervals. These two Reynolds numbers, together with the two Rossby numbers computed from  $\text{Ro} = \text{EkRe}$ , form endpoints of line segments in the  $(\text{Re}, \text{Ro})$ -plane which must be crossed by the stability limit of the 2D flows. These line segments are shown in the  $(\text{Re}, \text{Ro})$ -plane in fig. 5. For an alternative point of view, fig. 5 also shows the stability limit in the  $(\text{Ek}, \text{Ro})$ -plane. One can see that there is no unique critical Rossby number for the transition. The next section will show that the stability diagram in the  $(\text{Re}, \text{Ro})$ -plane can be explained by assuming that elliptical instability of the convection rolls is responsible for the transition.

#### IV. THE ELLIPTICAL INSTABILITY

A linear stability analysis of a convection roll in its rectangular cell requires a numerical effort comparable to the simulation of the original convection problem itself. It is more tractable and at the same time more illuminating to study the linear stability of a simplified flow using an approximate treatment of the boundaries.

As a simple model of the 2D laminar convection flow, we will consider a flow with elliptical

streamlines of the form  $((\gamma - \epsilon)z, 0, (-\gamma - \epsilon)x)$  in a frame of reference rotating at rate  $\Omega$  about the  $y$ -axis. The constants  $\gamma$  and  $\epsilon$  represent in dimensional variables a spatially uniform vorticity divided by 2 and a rate of strain, respectively. The streamlines of this flow are ellipses in the  $(x, z)$ -plane. The ratio of the large and small major axes of the ellipses is  $\alpha = \sqrt{(1 + \beta)/(1 - \beta)}$  with the definition  $\beta = \epsilon/\gamma$ . The calculation in this section parallels earlier work<sup>16-19</sup> except for the treatment of the boundaries.

We cannot treat the model with the same non dimensional variables as in the previous section because the thermal diffusivity is absent and there is no inherent length scale. We choose  $1/\gamma$  as time scale and express all lengths in terms of  $d$  which is arbitrary at present and which we will later identify with the size of the convection cell along the direction of gravity. Velocities are then given in multiples of  $\gamma d$ . Switching now to non dimensional variables, the elliptical base flow  $\mathbf{U}$  is given by

$$\mathbf{U} = \mathbf{A}\mathbf{r} \quad , \quad \mathbf{A} = \begin{pmatrix} 0 & 0 & 1 - \beta \\ 0 & 0 & 0 \\ -1 - \beta & 0 & 0 \end{pmatrix}. \quad (10)$$

The full velocity field  $\mathbf{u}$  is represented as the sum  $\mathbf{u} = \mathbf{U} + \mathbf{u}'$  of the base flow and the perturbation  $\mathbf{u}'$  which has to satisfy

$$\frac{\partial}{\partial t}\mathbf{u}' + (\mathbf{U} \cdot \nabla)\mathbf{u}' + (\mathbf{u}' \cdot \nabla)\mathbf{U} + (\mathbf{u}' \cdot \nabla)\mathbf{u}' + 2\omega\hat{\mathbf{y}} \times \mathbf{u}' = -\nabla p' + \eta\nabla^2\mathbf{u}' \quad (11)$$

$$\nabla \cdot \mathbf{u}' = 0 \quad (12)$$

where  $p'$  is a pressure variable,  $\omega = \Omega/\gamma$  is the non dimensional rotation rate of the frame of reference, and  $\eta = \nu/(\gamma d^2)$  quantifies viscous dissipation.

Eq. (11) is solved exactly by velocity and pressure fields of the form  $\mathbf{u}'(\mathbf{r}, t) = \mathbf{u}_0(t)e^{i\mathbf{k}(t)\cdot\mathbf{r}}$ ,  $p(\mathbf{r}, t) = p_0(t)e^{i\mathbf{k}(t)\cdot\mathbf{r}}$  provided that the time dependent amplitude  $\mathbf{u}_0(t)$  and the wavevector  $\mathbf{k}(t)$  obey

$$\frac{d}{dt}\mathbf{u}_0 + \mathbf{A}\mathbf{u}_0 + 2\omega\mathbf{u}_0 - 2\frac{\mathbf{k}\mathbf{k}^T}{|\mathbf{k}|^2}(\mathbf{A} + \omega)\mathbf{u}_0 + \eta|\mathbf{k}|^2\mathbf{u}_0 = 0 \quad (13)$$

$$\frac{d}{dt}\mathbf{k} + \mathbf{A}^T\mathbf{k} = 0 \quad (14)$$

with the definition

$$\omega = \begin{pmatrix} 0 & 0 & \omega \\ 0 & 0 & 0 \\ -\omega & 0 & 0 \end{pmatrix}. \quad (15)$$

It follows directly from eq. (14) that the  $y$ -component of  $\mathbf{k}$  is independent of time and that the vector  $\mathbf{k}$  precesses elliptically about the  $y$ -axis. One can thus assume without loss of generality initial conditions for  $\mathbf{k}$  of the form

$$\mathbf{k}(t=0) = k_0 \begin{pmatrix} 0 \\ \cos \theta \\ \sin \theta \end{pmatrix} \quad (16)$$

with arbitrary  $k_0$  and  $\theta$ . At later times, the wavevector is determined by eq. (14) to be

$$\mathbf{k}(t) = k_0 \begin{pmatrix} \alpha \sin \theta \sin(\sqrt{1-\beta^2}t) \\ \cos \theta \\ \sin \theta \cos(\sqrt{1-\beta^2}t) \end{pmatrix}. \quad (17)$$

This expression for  $\mathbf{k}$  inserted into eq. (13) leads to a linear ordinary differential equation for  $\mathbf{u}_0$  with time periodic coefficients. This is a problem which can be reduced to an algebraic eigenvalue problem following the method detailed in refs.<sup>16-18</sup> of which we provide a succinct summary for completeness: In a first step, the viscous term is removed from the equations by introducing a new variable  $\tilde{\mathbf{u}}_0$  as

$$\tilde{\mathbf{u}}_0 = e^{\eta \int_0^t |\mathbf{k}|^2 dt} \mathbf{u}_0 \quad (18)$$

which transforms eq. (13) into

$$\frac{d}{dt} \tilde{\mathbf{u}}_0 = \mathbf{Q}(t) \tilde{\mathbf{u}}_0 \quad , \quad \mathbf{Q}(t) = 2 \frac{\mathbf{k} \mathbf{k}^T}{|\mathbf{k}|^2} (\mathbf{A} + \boldsymbol{\omega}) - (\mathbf{A} + 2\boldsymbol{\omega}). \quad (19)$$

The general solution of this equation may be deduced from the Floquet problem

$$\frac{d}{dt} \mathbf{M} = \mathbf{Q}(t) \mathbf{M} \quad , \quad \mathbf{M}(t=0) = \mathbf{1}, \quad (20)$$

the general solution for  $\tilde{\mathbf{u}}_0$  being a linear combination of functions of the form

$$\tilde{\mathbf{u}}_0(t) = e^{\sigma_i t} \mathbf{f}_i(t) \quad (21)$$

where the  $\mathbf{f}_i(t)$ ,  $i = 1, 2, 3$  are periodic functions with period  $2\pi/\sqrt{1-\beta^2}$  and the  $\sigma_i$  are given by

$$\sigma_i = \frac{\sqrt{1-\beta^2}}{2\pi} \ln \mu_i \quad (22)$$

where the  $\mu_i$  are the three eigenvalues of  $\mathbf{M}$  at  $t = 2\pi/\sqrt{1-\beta^2}$ . One can show that one of the eigenvalues equals 1, say  $\mu_3 = 1$ , and the other two eigenvalues obey  $\mu_1\mu_2 = 1$ . If there are growing solutions, one has  $\mu_2 < 1 < \mu_1$  and the fastest growing mode has the growth rate  $\sigma_1 = \frac{\sqrt{1-\beta^2}}{2\pi} \ln \mu_1$ . We now reinstate viscous dissipation with the help of the integral

$$-\eta \int_0^{2\pi/\sqrt{1-\beta^2}} |\mathbf{k}|^2 dt = -\eta k_0^2 \left( 1 + \frac{1}{2}(\alpha^2 - 1) \sin^2 \theta \right). \quad (23)$$

The growth rate  $\sigma$  of the fastest growing solution  $\mathbf{u}_0$  of eq. (13) is therefore

$$\sigma = \frac{1}{2\pi} \left( \frac{\sqrt{1-\beta^2}}{2\pi} \ln \mu_1 - 2\pi\eta k_0^2 \frac{1-\beta \cos^2 \theta}{1-\beta} \right). \quad (24)$$

This equation yields a growth rate for any given  $\omega$ ,  $\eta$ ,  $\beta$  and  $k_0$  after a numerical time integration of eq. (20) up to  $t = 2\pi/\sqrt{1-\beta^2}$  followed by a numerical evaluation of the eigenvalues of  $\mathbf{M}$ .

At this stage of the calculation, we make a different use of eq. (24) than previous papers which derived this relation. It is now possible to identify control parameters which yield solutions growing in time and to find for any fixed  $\beta$  and  $\omega$  the largest  $\eta$  that still allows for growing solutions by optimizing over  $k_0$  and  $\theta$ . However, in order to reproduce the results of the time integrations of the previous section, it is necessary to model the effect of the boundaries. This is done by restricting  $k_0$  and  $\theta$  to combinations which satisfy

$$k_0 \cos \theta \geq k_{\parallel} \quad , \quad k_0 \sin \theta \geq k_{\perp}. \quad (25)$$

The rationale behind this condition is that the normal velocity at the boundaries of the cell must be zero and that therefore at least half a wavelength must fit into the cell. This condition applied to the direction along the rotation axis leads to  $k_{\parallel} = 2\pi$ . Likewise, the components of  $\mathbf{k}$  perpendicular to the axis of rotation, taking into account the factor  $\alpha$  in the  $x$ -component of (17), must be larger than  $\pi$  to fit half a wavelength into a cell of the geometry chosen for the direct simulations, so that  $k_0$  must also satisfy  $k_0 \sin \theta \geq \pi$  which implies  $k_{\perp} = \pi$ . The conditions (25) are not exactly equivalent to the free slip boundaries of the simulations, but they suffice to represent the geometric constraints imposed by the finite size of the convection cell as we shall see.

If we apply the definition (6) for the Reynolds number to the elliptical flow taking into account that the scales for the non dimensional velocities are different, we compute

$$4 \int_{-1/4}^{1/4} dx \int_{-1/4}^{1/4} dy \int_{-1/2}^{1/2} dz [(1-\beta)^2 z^2 + (1+\beta)^2 x^2] = \frac{1}{12} \left[ (1-\beta)^2 + \frac{1}{4}(1+\beta)^2 \right] \quad (26)$$

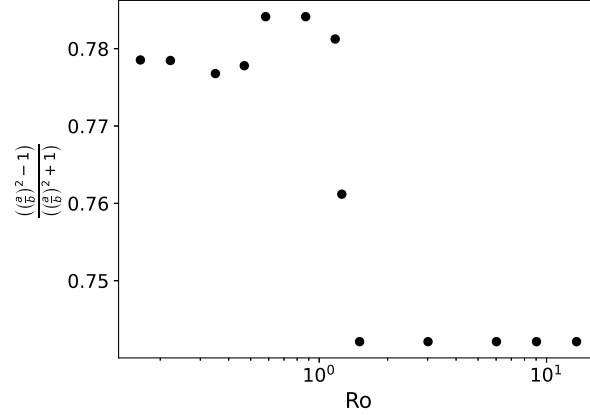


FIG. 6. Ellipticities of the streamlines of 2D convection flows at the center of the cell deduced from the eigenvalues  $1/a$  and  $1/b$  of the Jacobian of the velocity field. Ellipticity is defined as the parameter  $\beta$  in eq. (10).

and conclude that we have to compare a simulation at a certain  $Re$  and  $Ro$  with a purely elliptical flow parameterized with  $\eta$ ,  $\omega$  and  $\beta$  such that

$$Re = \frac{1}{\eta} \sqrt{\frac{1}{12} \left[ (1 - \beta)^2 + \frac{1}{4}(1 + \beta)^2 \right]} \quad (27)$$

and

$$Ro = \frac{1}{\omega} \sqrt{\frac{1}{12} \left[ (1 - \beta)^2 + \frac{1}{4}(1 + \beta)^2 \right]}. \quad (28)$$

It remains to select a  $\beta$  to completely specify the stability limit. Fig. 5 shows the stability limit in the  $(Re, Ro)$ -plane for  $\beta = 0.78$  which is already a reasonable fit to the simulation data considering all the simplifications introduced into the model of purely elliptical streamlines.

A simple estimate of  $\beta$  in which the major axes of the ellipse are set equal to the length of the sides of the convection cell yields  $\beta = 0.6$ . While the streamlines of the convection roll espouse the shape of the cell near the boundaries of the cell, the ellipticity of these streamlines near the center of the cell is uncertain. We therefore compute the eigenvalues of the Jacobian of the velocity field at the center of the cell for the 2D flows next to the transition. For exactly elliptical streamlines, these eigenvalues are the inverse of the semi major axes. One of the three eigenvalues is zero in 2D flows. If we call the smaller of the remaining eigenvalues  $1/a$  and the last one  $1/b$ , we can compute an approximate  $\beta$  as  $[(a/b)^2 - 1] / [(a/b)^2 + 1]$ . This combination is shown in fig. 6 as a function of  $Ro$ . The value

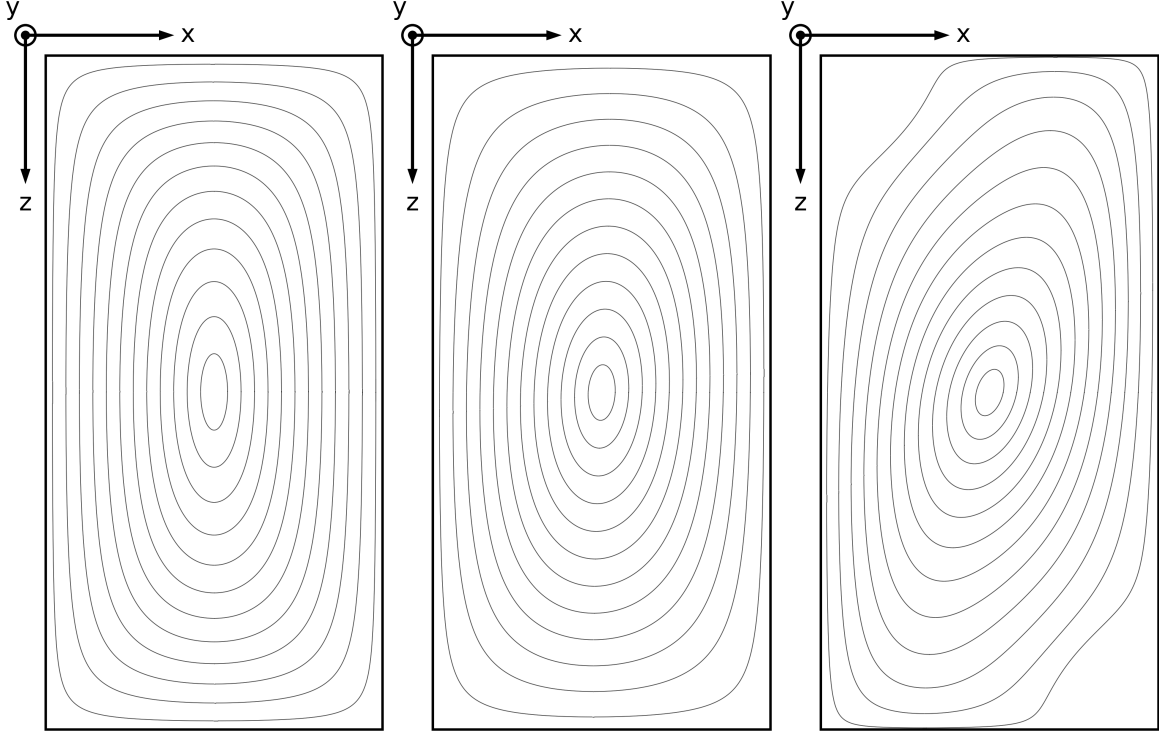


FIG. 7. Streamlines of the two dimensional flows at  $\text{Ek} = 4 \times 10^{-5}$  and  $\text{Ra} = 8 \times 10^6$  corresponding to  $\text{Ro} = 6.6 \times 10^{-2}$  (left panel),  $\text{Ek} = 7 \times 10^{-3}$  and  $\text{Ra} = 10^5$  corresponding to  $\text{Ro} = 1.24$  (middle panel) and  $\text{Ek} = 9 \times 10^{-2}$  and  $\text{Ra} = 8 \times 10^4$  corresponding to  $\text{Ro} = 13.3$  (right panel).

changes abruptly near  $\text{Ro} \approx 1$ . The change is relatively small in absolute value and barely visible in plots of streamlines (see fig. 7). The 2D flow is of course insensitive to rotation and the change in the flow pattern is due to the different Rayleigh numbers for the flows close to the transition. Even though the changes in the surrogate  $\beta$  are small, its systematic variation with  $\text{Ro}$  justifies the use of two different  $\beta$  for the model elliptical flow at either large or small  $\text{Ro}$ .

In addition to using two different  $\beta$ , there are more refinements that are possible to improve the stability line in fig. 5. Visualisations of the velocity field just above onset computed in the previous section show that the fastest growing mode prefers to fit a full wavelength into the cell in the plane perpendicular to the rotation axis so that we may set  $k_{\perp} = 2\pi$ . Furthermore, since the conditions (25) reproduce only approximately the effect of free slip boundaries, we may consider  $k_{\parallel}$  or  $k_{\perp}$  to be fit parameters. Leaving  $k_{\perp}$  at  $2\pi$  and slightly adjusting  $k_{\parallel}$  to  $5\pi/3$  leads to fig. 8. While these adjustments of course improve the fit, it should be noted that the straightforward choice of parameters in fig. 5 suffices

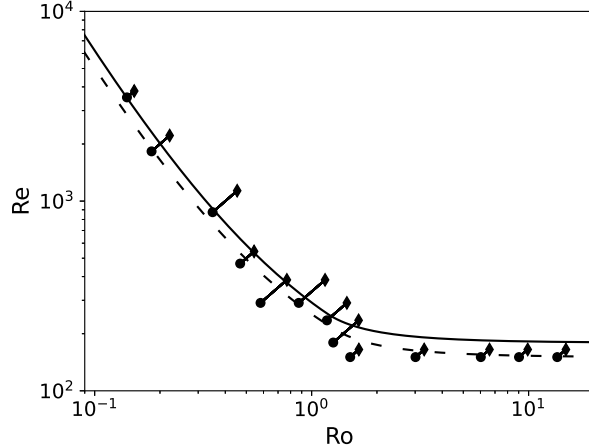


FIG. 8. The stability limit of an elliptical vortex computed for  $k_{\parallel} = 5\pi/3$ ,  $k_{\perp} = 2\pi$  and  $\beta = 0.8$  (solid line, intended as a fit at small  $Ro$ ) or  $\beta = 0.76$  (dashed line, intended as a fit at large  $Ro$ ) together with the same numerical data as in fig. 5 delimiting the stability limit of 2D convection flow.

to reproduce the general appearance of the stability curve and that the more refined choice only leads to minor modifications, separately at large and small  $Ro$ .

The values of  $[(a/b)^2 - 1] / [(a/b)^2 + 1]$  in fig. 6 are maximal around  $Ro \approx 1$  and it is precisely at this  $Ro$  that the lines drawn in fig. 8 fail to reproduce well the correct stability limit. The correlation between the transition from 2D to 3D in the simulated convection flow and the onset of elliptical instability deduced from  $[(a/b)^2 - 1] / [(a/b)^2 + 1]$  supports the claim that this transition is due to an elliptical instability of the convection roll.

It is crucial to account for a finite cell size through condition (25) to reproduce the correct stability limit. To gain insight into the role of this condition, it is instructive to look at eqs. (14, 13) in a limit in which asymptotically correct solutions can be obtained analytically<sup>18–20</sup>, which is the double limit of  $\beta \ll 1$  and  $\omega \gg 1$ . To perform the calculation,  $\mathbf{u}_0$  is expanded in a series in  $\beta$  as

$$\mathbf{u}_0 = [\mathbf{w}_0(t) + \beta\mathbf{w}_1(t) + \mathcal{O}(\beta^2)] e^{\sigma t}. \quad (29)$$

This expansion is inserted into the energy equation derived from eq. (13) by taking the dot product of this equation with  $\mathbf{u}_0$ :

$$\frac{1}{2} \frac{d}{dt} \mathbf{u}_0^2 = -\mathbf{u}_0(\mathbf{A} + 2\boldsymbol{\omega})\mathbf{u}_0 - \eta|\mathbf{k}|^2|\mathbf{u}_0|^2. \quad (30)$$

The problem for  $\beta = 0$  is solved by

$$\mathbf{w}_0 = \frac{1}{2} e^{-\eta k_0^2 t} \begin{pmatrix} -(1 - \cos \theta) \sin(\Gamma_+ t + \phi) - (1 + \cos \theta) \sin(\Gamma_- t + \phi) \\ -2 \sin \theta \sin(\Gamma t + \phi) \\ -(1 - \cos \theta) \cos(\Gamma_+ t + \phi) + (1 + \cos \theta) \cos(\Gamma_- t + \phi) \end{pmatrix} \quad (31)$$

where  $\phi$  is an arbitrary phase and  $\Gamma_{\pm} = \Gamma \pm 1$  with

$$\Gamma = 2(1 + \omega) \cos \theta. \quad (32)$$

Inserting this expression into the right hand side of eq. (30) yields to leading order in  $\beta$ :

$$\sigma = \frac{\beta}{4} [(1 - \cos \theta)^2 \sin[2(\Gamma_+ t + \phi)] - (1 + \cos \theta)^2 \sin[2(\Gamma_- t + \phi)] - 2(1 - \cos^2 \theta) \sin(2t)] - \eta k_0^2. \quad (33)$$

The average of  $\sigma$  over long time intervals vanishes unless  $\Gamma_+$  or  $\Gamma_-$  is zero, in which case the maximal growth rate is

$$\sigma = \frac{\beta}{16} \frac{(3 + 2\omega)^2}{(1 + \omega)^2} - \eta k_0^2. \quad (34)$$

This growth rate in turn is maximized by the smallest admissible  $k_0^2$ . In an infinitely extended vortex,  $k_0^2$  could be arbitrarily small and viscosity would be irrelevant for the stability of the vortex. However,  $k_0^2$  is limited in the present application by either the boundaries or the finite size of the convection rolls. If we naively require  $k_0^2 > k_{\min}^2$ , a positive growth rate is obtained in eq. (34) for  $\eta < \beta / (2k_{\min})^2$  at large  $\omega$ , which corresponds to a fixed critical Reynolds number at small Rossby numbers and which is not at all the behaviour observed in the simulations. On the other hand, the more detailed condition (25) with  $k_{\parallel} = 2\pi$  imposes  $k_0^2 \geq 4\pi^2 / \cos^2 \theta$ , which because of eq. (32) and either  $\Gamma_+$  or  $\Gamma_-$  being zero leads to  $k_0^2 \geq 16\pi^2(1 + \omega)^2$ . Inserting this expression into eq. (34) and setting  $\sigma = 0$  to find the stability limit, we obtain

$$\frac{\beta}{16} \frac{(3 + 2\omega)^2}{(1 + \omega)^2} = 16\pi^2 \eta (1 + \omega)^2 \quad (35)$$

which in the limit of large  $\omega$  is equivalent to

$$\frac{1}{\eta} = \frac{64}{\beta} \pi^2 \omega^2. \quad (36)$$

Translated to Rossby and Reynolds numbers, this relation implies that  $\text{Re} \propto \text{Ro}^{-2}$  at the onset of instability which is close to what is observed in the simulations. Apparently, it is the limited extent of the convection roll along its axis which is responsible for the right hand side in eq. (35) and the observed variation of the Rossby number at the transition.



One can also deduce from this derivation why the flow can become 3D despite  $Ro$  being small. A small  $Ro$  guarantees the advection term to be small compared with the Coriolis term in the Navier-Stokes equation if both terms are computed for the base flow. The wavenumber introduced by the instability,  $k_0$ , behaves for large  $\omega$  as  $k_0 \sim 4\pi\omega$ . The magnitude of the second term in eq. (11),  $(\mathbf{U} \cdot \nabla)\mathbf{u}'$ , is then proportional to  $|\mathbf{u}'|\omega$  and hence comparable to the Coriolis term in eq. (11),  $2\omega\hat{\mathbf{y}} \times \mathbf{u}'$ . Similarly, the time derivative  $\frac{\partial}{\partial t}\mathbf{u}'$  is also comparable to the Coriolis term in this case. The geostrophic balance, which requires that only the pressure gradient be comparable to the Coriolis term in eq. (11) and which implies 2D flows, is thus broken because the instability occurs on a length scale which varies as the inverse of  $\omega$ .

## V. CONCLUSION

This study was triggered by the advent of experiments which use centrifugal acceleration to create a large effective gravity inside a convection cell. The rotation also favors 2D flow structures. Global quantities like the heat flux scale differently in 2D and 3D flows so that it becomes important to know under which conditions the 2D convection is replaced by 3D convection.

A comparison of time scales associated with rotation and buoyancy suggests that buoyancy is irrelevant to the transition from 2D to 3D flows. However, this transition does not occur at a specific Rossby number independent of other control parameters. The transition is due to an elliptic instability of the convection rolls. This confirms that buoyancy is irrelevant to the transition. It also implies that a finite viscosity is not necessary for the instability since the elliptical instability is an inertial instability. On the other hand, viscosity together with a finite extent of the convection rolls leads to a Reynolds number dependent Rossby number at the transition. In the simulations and in the experiment by Menaut *et al.*<sup>2</sup> the convection rolls are confined by sidewalls. However, even in an annular geometry, the lateral roll size is finite and is for example limited by the critical wavenumber near the onset so that the volume of fluid exposed to the basic elliptical flow is restricted. According to an analytic calculation valid in the limit of small ellipticity and Rossby number, it is at any rate the size restriction along the roll axis which is essential and which leads to the relation  $Re \propto Ro^{-2}$  at the transition.

The experiments performed so far do not provide us with enough information about

the velocity field to conclusively test the scenario of the elliptical instability. Note that the Rossby number in Jiang *et al.*<sup>1</sup> is based on the computed free fall velocity and not on an actual measured velocity. The comparison of simulations and experiments in the (Ra, Ek)–plane is not helpful because it depends on the Re(Ra) relation which is affected by the cylindrical geometry in the experiment by Jiang *et al.*<sup>1</sup> and by compressibility in the experiment by Menaut *et al.*<sup>2</sup>. However, compressibility is not expected to modify the stability criterion in the (Re, Ro)–plane because it was found that the criterion for elliptical instability is independent of compressibility in spheroidal geometry<sup>21</sup>. Measurements of temperature and pressure fluctuations allow Menaut *et al.*<sup>2</sup> to determine which of their flows are 2D. These authors estimate velocity assuming either a balance between pressure gradient and Coriolis acceleration or between pressure gradient and the advection term in the momentum equation and find Rossby numbers of 0.01 and 0.1, respectively. Starting from the Rossby number deduced from the assumption of a geostrophic equilibrium and Ekman numbers in the range  $10^{-7} - 10^{-6}$  typical of the experiments, one obtains Reynolds numbers in between  $10^4$  and  $10^5$ , which means that  $\text{Re} < 100\text{Ro}^{-2}$  is obeyed. The stability limit of the numerical simulations at low Rossby numbers is approximately given by  $\text{Re} \approx 100\text{Ro}^{-2}$ . In as far as a quantitative comparison is possible, theory and experiment agree on the prevalence of 2D flows in nearly geostrophic equilibrium in the experiments by Menaut *et al.*<sup>2</sup>.

## ACKNOWLEDGMENTS

The authors acknowledge the help by Marie-Christine Volk who computed the 2D results shown in figs. 1, 2 and 6 as part of her Bachelor’s thesis. This work was funded by the Deutsche Forschungsgemeinschaft (DFG) under the grant Ti 243/13.

## REFERENCES

- <sup>1</sup>H. Jiang, X. Zhu, D. Wang, S. G. Huisman, and C. Sun, “Supergravitational turbulent thermal convection,” *Science Advances* **6**, eabb8676 (2020).
- <sup>2</sup>R. Menaut, Y. Corre, L. Huguet, T. Le Reun, T. Alboussière, M. Bergman, R. Deguen, S. Labrosse, and M. Moulin, “Experimental study of convection in the compressible regime,” *Phys. Rev. Fluids* **4**, 033502 (2019).

- <sup>3</sup>S. Schmitz and A. Tilgner, “Heat transport in rotating convection without Ekman layers,” *Phys. Rev. E* **80**, 015305(R) (2009).
- <sup>4</sup>S. Schmitz and A. Tilgner, “Transitions in turbulent rotating Rayleigh-Bénard convection,” *Geophys. Astrophys. Fluid Dyn.* **104**, 481–489 (2010).
- <sup>5</sup>L. Zwirner, A. Tilgner, and O. Shishkina, “Elliptical Instability and Multiple-Roll Flow Modes of the Large-Scale Circulation in Confined Turbulent Rayleigh-Bénard Convection,” *Phys. Rev. Lett.* **125**, 054502 (2020).
- <sup>6</sup>Q. Wang, R. Verzicco, D. Lohse, and O. Shishkina, “Multiple states in turbulent large-aspect-ratio thermal convection: What determines the number of convection rolls?” *Phys. Rev. Lett.* **125**, 074501 (2020).
- <sup>7</sup>V. Tanriverdi and A. Tilgner, “Global fluctuations in magnetohydrodynamic dynamos,” *New Journal of Physics* **13**, 033019 (2011).
- <sup>8</sup>A. Tilgner, “Transitions in rapidly rotating convection dynamos,” *Phys. Rev. Lett.* **109**, 248501 (2012).
- <sup>9</sup>B. Wen, D. Goluskin, M. LeDuc, G. P. Chini, and C. R. Doering, “Steady Rayleigh-Bénard convection between stress-free boundaries,” *Journal of Fluid Mechanics* **905**, R4 (2020).
- <sup>10</sup>E. P. van der Poel, R. Ostilla-Mónico, R. Verzicco, and D. Lohse, “Effect of velocity boundary conditions on the heat transfer and flow topology in two-dimensional Rayleigh-Bénard convection,” *Phys. Rev. E* **90**, 013017 (2014).
- <sup>11</sup>Q. Wang, K. L. Chong, R. J. A. M. Stevens, R. Verzicco, and D. Lohse, “From zonal flow to convection rolls in Rayleigh-Bénard convection with free-slip plates,” *Journal of Fluid Mechanics* **905**, A21 (2020).
- <sup>12</sup>A. Pandey, A. Kumar, A. G. Chatterjee, and M. K. Verma, “Dynamics of large-scale quantities in Rayleigh-Bénard convection,” *Phys. Rev. E* **94**, 053106 (2016).
- <sup>13</sup>A. Rouhi, D. Lohse, I. Marusic, C. Sun, and D. Chung, “Coriolis effect on centrifugal buoyancy-driven convection in a thin cylindrical shell,” *Journal of Fluid Mechanics* **910**, A32 (2021).
- <sup>14</sup>J.-Q. Zhong, R. J. A. M. Stevens, H. J. H. Clercx, R. Verzicco, D. Lohse, and G. Ahlers, “Prandtl-, Rayleigh-, and Rossby-Number Dependence of Heat Transport in Turbulent Rotating Rayleigh-Bénard Convection,” *Phys. Rev. Lett.* **102**, 044502 (2009).
- <sup>15</sup>S. Horn and O. Shishkina, “Toroidal and poloidal energy in rotating Rayleigh-Bénard convection,” *Journal of Fluid Mechanics* **762**, 232–255 (2015).

- <sup>16</sup>B. Bayly, “Three-dimensional instability of elliptical flow,” *Phys. Rev. Lett.* **57**, 2160–2163 (1986).
- <sup>17</sup>M. Landmann and P. Saffman, “The three-dimensional instability of strained vortices in a viscous fluid,” *Phys. Fluids* **30**, 2339–2342 (1987).
- <sup>18</sup>A. Craik, “The stability of unbounded two- and three-dimensional flows subject to body forces: some exact solutions,” *J. Fluid Mech.* **198**, 275–292 (1989).
- <sup>19</sup>R. Kerswell, “Elliptical instability,” *Annu. Rev. Fluid Mech.* **34**, 83–113 (2002).
- <sup>20</sup>F. Waleffe, “On the three-dimensional instability of strained vortices,” *Phys. Fluids A* **2**, 76–80 (1990).
- <sup>21</sup>N. Clausen and A. Tilgner, “Elliptical instability of compressible flow in ellipsoids,” *Astron. Astrophys.* **562**, A25 (2014).